crystals

MDPI

Article

Phase Structures and Dielectric Properties of $(n + 1)SrO - nCeO_2$ ($n = 2$) Microwave Ceramic Systems with TiO_2 Addition

Qi Su [1], Jingjing Qu [2,3,*], Fei Liu [1,*], Changlai Yuan [4], Xiao Liu [4], Mingwei Su [4], Liufang Meng [4] and Guohua Chen [4]

[1] School of Mechanical and Electrical Engineering, Guilin University of Electronic Technology, Guilin 541004, China; suqi0940915@163.com
[2] School of Electronic Engineering Automation, Guilin University of Electronic Technology, Guilin 541004, China
[3] School of Mechanical and Electrical Engineering, Guilin University of Aerospace Technology, Guilin 541004, China
[4] Guangxi Key Laboratory of Information Materials, Guilin University of Electronic Technology, Guilin 541004, China; yclai-2002@163.com (C.Y.); a4718412471@163.com (X.L.); sumingwei2022@163.com (M.S.); mlf_2019@163.com (L.M.); cgh1682002@163.com (G.C.)
* Correspondence: qujingjing@guat.edu.cn (J.Q.); liufeiguet@163.com (F.L.)

Abstract: Ti^{4+}-ion-doped $(n + 1)SrO - nCeO_2$ ($n = 2$) ceramic systems were prepared with the conventional solid-state reaction method, and the effects of the phase structures and compositions, sintering behaviors, microstructures and microwave dielectric properties of these ceramic systems were investigated in detail as a function of TiO_2 content. The analytical results of the XRD patterns show that the pure $(n + 1)SrO - nCeO_2$ ($n = 2$) system is a composite-phase ceramic system with coexisting $SrCeO_3$ and Sr_2CeO_4 phases (represented as a $SrCeO_3 + Sr_2CeO_4$ system), which belong to the orthogonal structures of the Pmcn (62) and Pbam (55) space groups, respectively. For the $xTiO_2$-(1 − x) ($SrCeO_3 + Sr_2CeO_4$) ($x = 0.1$–0.4) ceramic samples, the secondary phase Sr_2TiO_4 can also be detected within the range of the investigated components. Meanwhile, the Raman spectroscopy, SEM-EDS, and HRTEM (SAED) analysis results also verified the correctness and consistency of the phase structures and compositions for all the given specimens. In addition, complex impedance spectroscopy was used to detect the conductive behavior of these compound ceramic systems, and the calculation results show that the appropriate addition of Ti^{4+}-ions can make the $SrCeO_3 + Sr_2CeO_4$ system have better thermal stability. The composition of $x = 0.2$ multiphase structural ceramic sample sintered at 1330 °C for 4 h has a near zero τ_f value of ~−4.6 ppm/°C, a moderate ε_r of ~40.3 and a higher $Q \times f$~44,020 GHz (at 6.56 GHz). The relatively superior-performing ceramics developed in this work are expected to provide a promising microwave dielectric material for communication components.

Keywords: phase structures and compositions; $SrCeO_3 + Sr_2CeO_4$ system; TiO_2 addition; microwave dielectric properties

Citation: Su, Q.; Qu, J.; Liu, F.; Yuan, C.; Liu, X.; Su, M.; Meng, L.; Chen, G. Phase Structures and Dielectric Properties of $(n + 1)SrO - nCeO_2$ ($n = 2$) Microwave Ceramic Systems with TiO_2 Addition. *Crystals* **2023**, *13*, 955. https://doi.org/10.3390/cryst13060955

Academic Editor: Artem Pronin

Received: 9 May 2023
Revised: 2 June 2023
Accepted: 13 June 2023
Published: 15 June 2023

1. Introduction

For the fifth generation (5G) and the sixth generation (6G) of communication technology, much of the future research will focus on the development of millimeter wave frequency bands from centimeter waves to the higher frequencies, which requires microwave devices to have higher transmission rates and mobility performance and lower signal delay. Dielectric ceramics in microwave devices are considered important matrix materials that can achieve all the aforementioned advantages simultaneously. With the gradual development of electronic information and communication technology in modern society, the application scenarios of microwave dielectric ceramics (MWDCs) have become

closely related to our lives [1–4], especially in the development of communication devices such as filters, dielectric resonators, duplexers, dielectric antennas, dielectric substrates, and radar satellites, etc. [5–8]. Among them, the current usage of filters is particularly prominent. With the emergence of 5G and 6G environments, communication devices such as base stations and mobile phones have entered the era of the Internet of Everything (MIMO). As the number of base station deployments continues to surge, the usage of filters and other devices is also increasing. As the matrix material, microwave dielectric ceramics will also face huge challenges in their performance in terms of the relative dielectric constant (ε_r), quality factor multiplied by resonant frequency ($Q \times f$) and temperature coefficient of the resonant frequency (τ_f). In general, for the regulation of microwave dielectric properties, based on the determination of ε_r value for its use in functional microwave devices, the objective of optimization is a higher $Q \times f$ value, and a τ_f value closer to zero [9–12]. This also puts forward new requirements for the performance of microwave dielectric ceramics such as the filters' base materials, including a lower dielectric loss (higher quality factor), good thermal stability (a near-zero τ_f value) and a moderate ε_r value. This not only ensures device miniaturization, but also meets the requirements of the low signal delay [13–16]. Therefore, to enrich the serialized microwave dielectric properties, researchers need to continue to explore the different ceramic systems, of which the ABO_3-type perovskite and multiphase materials are the most widely studied.

In our previous studies, a pure $SrCeO_3$ ceramic sample sintered at 1350 °C for 4 h could obtain relatively superior microwave dielectric properties: ε_r = 48.2, $Q \times f$ = 22,160 GHz (at 6.06 GHz) and τ_f = −43.6 ppm/°C [17]. The ε_r value of this ceramic is between 40 and 50, which means it belongs to the category of intermediate electric (20–60) microwave ceramic systems, but there is still a certain gap from the practical range. It therefore needs to further enhance its $Q \times f$ value and regulate the τ_f value to near zero (-10 ± 10 ppm/°C). Moreover, other previous reports in the literature have focused on the microwave dielectric properties of the Sr_2CeO_4 [$(n + 1)SrO - nCeO_2$ (n = 1)] ceramic system. Dai et al. successfully prepared Sr_2CeO_4 solid solution ceramics, and found that a sample sintered at 1270 °C for 4 h could obtain the optimal microwave dielectric properties: τ_f = −62 ppm/°C, $Q \times f$ = 172,600 GHz (at 9.4 GHz) and ε_r = 15 [18]. It can be seen that the Sr_2CeO_4 ceramic sample has a high $Q \times f$ value and the same orthotropic structure as the pure $SrCeO_3$ ceramic; thus, it is expected that the pure $SrCeO_3$ matrix can be compounded with the Sr_2CeO_4 system to enhance the $Q \times f$ value in the new composite ceramic systems. At the same time, it has been confirmed that the addition of Ti^{4+}-ions can indeed regulate the thermal stability of these $SrCeO_3$-based and Sr_2CeO_4-based ceramic systems [17,18].

Based on the above analysis, this work attempts to prepare a composite of $(n + 1)SrO - nCeO_2$ (n = 2) ceramic systems through the traditional solid-state method, and aims to explore the phase structures and compositions of the new microwave ceramic systems. Additionally, the dielectric properties of these new ceramic systems are further optimized by adding different Ti^{4+}-ion contents. The internal correlation among the crystal structures, microstructures, crystal structures, conductive behaviors and microwave dielectric properties is also systematically analyzed in this work.

2. Materials and Methods

The $(n + 1)SrO - nCeO_2$ (n = 2) and the $x TiO_2$-(1 − x) ($SrCeO_3 + Sr_2CeO_4$) (x = 0.1–0.4) ceramic specimens were synthesized using the traditional solid-state reaction method with $SrCO_3$ (≥99.95%, Shanghai Aladdin Biochemical Technology Co., Ltd., Shanghai, China), CeO_2 (≥99.9%, Shanghai Maclean Biochemical Technology Co., Ltd., Shanghai, China) and TiO_2 (≥99.99%, Shanghai Aladdin Biochemical Technology Co., Ltd., Shanghai, China). The high-purity powder was weighed according to the stoichiometric ratio, and placed in a nylon tank containing zirconia balls and anhydrous ethanol as the ball milling medium on the ball mill for 24 h. The slurry was allowed to dry completely in an oven at 90 °C, then it was sieved through a 100 mesh sieve. After calcination in a muffle furnace at 1100 °C for 6 h, the mixed powder was finely ground for 0.5–1 h and granulated by adding 5 wt%

polyvinyl alcohol. The prepared mixed powder was pressed into cylindrical embryos (12 mm diameter and 5–6 mm thickness) under a uniaxial pressure of 300 MPa. Finally, these ceramic embryos were calcined in a muffle furnace at 600 °C for 2 h to precipitate adhesive, and sintered at 1310–1410 °C for 4 h at a rate of 2 °C/min to obtain dense ceramic samples.

The bulk density of the $(n + 1)SrO - nCeO_2$ ($n = 2$) and $xTiO_2$-$(1 - x)$ $(SrCeO_3 + Sr_2CeO_4)$ (x = 0.1–0.4) ceramic samples was measured using the Archimedes method. The phase structures and compositions of the sintered samples at room temperature were examined using X-ray diffraction (XRD, NEW Smartlab, Japan) equipped with a Cu-Kα (1.5406 Å) radiation instrument in the range of 2θ = 10–90°. A Raman spectrometer (Horiba JY, France) was used to detect the Raman spectra changes in the range of 50–900 cm^{-1} at room temperature, and to analyze the vibration mode changes of ceramic samples. The surface morphology and element distribution of ceramic samples were recorded using scanning electron microscopy (SEM, JSM7610FPlus, Japan) and energy-dispersive X-ray spectroscopy (EDS). The partially given samples were examined with high resolution transmission electron microscopy (HRTEM) and selected-area electron diffraction (SAED) to further analyze their structures. The impedance analyzer (Agilent 4294A, USA) was used to investigate the different conductivity characteristics of grains, grain boundaries and interfaces in the polycrystalline bulk ceramics. The vector network analyzer (E5230C, Agilent, USA) was used to measure the microwave dielectric properties of the sintered samples. The ε_r values were recorded by using the Hakki–Coleman method in TE_{011} resonant mode at microwave frequencies of 5.5–7.3 GHz, and the Q values were measured using the resonant cavity method [19]. The values of τ_f were measured at 25–75 °C (frequency range 5.5–6.8 GHz) by using the parallel plate method and calculated through the following equation [20,21]:

$$\tau_f = \frac{\Delta f_0}{f_0 \Delta T} = \frac{f_{75} - f_{25}}{f_{25} \times 50} \quad (1)$$

where f_{75} and f_{25} represent the resonant frequencies at 75 °C and 25 °C, respectively.

3. Results

Figure 1a shows the room temperature XRD patterns of the $(n + 1)SrO - nCeO_2$ ($n = 2$) ceramics sintered at 1330–1410 °C for 4 h. All observed XRD diffraction peaks conform to the orthogonal structure of standard PDF cards JCPDS # 89-5546 and JCPDS # 82-2427 [22,23]. Thus, the $(n + 1)SrO - nCeO_2$ ($n = 2$) ceramics cannot form a layered solid solution phase while forming a composite-phase ceramic system with the coexistence of a $SrCeO_3$ phase and a Sr_2CeO_4 phase; these two main crystalline phases belong to the orthogonal structure of Pmcn (62) and Pbam (55) space group, respectively. Figure 1b indicates the magnified XRD diffraction pattern at 2θ = 28–31°. As the sintering temperature increases, the positions of the main peaks of these two phases are basically unchanged and the peak intensities always remain relatively high, further indicating that $SrCeO_3$ and Sr_2CeO_4 phases can be formed and remain stable at different sintering temperatures for the $(n + 1)SrO - nCeO_2$ ($n = 2$) ceramic samples. These analysis results comprehensively indicate that $(n + 1)SrO - nCeO_2$ ($n = 2$) ceramics are a composite phase composed of $SrCeO_3$ and Sr_2CeO_4 phases, and can be expressed as the $SrCeO_3 + Sr_2CeO_4$ composite ceramic system in subsequent statements.

Figure 2a shows the XRD diffraction peaks of the $xTiO_2$-$(1 - x)$ $(SrCeO_3 + Sr_2CeO_4)$ (x = 0.1–0.4) ceramics sintered at 1350 °C for 4 h. Most major characteristic peaks (110), (011), (211), (111), (021), (221), (231), (422) and (360) can be matched with the standard PDF cards (JCPDS # 89-5546 and JCPDS # 82-2427), which is in good agreement with the two main phases of $SrCeO_3$ and Sr_2CeO_4 in Figure 1. At the same time, another second phase of Sr_2TiO_4 can be detected based on the PDF card JCPDS # 39-1471 within the range of the investigated components [24,25]. Figure 2b displays the XRD diffraction patterns in the range of 2θ = 28.5–33°. Due to the different radii of Ti^{4+}-ions (0.605 Å) and Ce^{4+}-ions (0.87 Å), the relatively small Ti^{4+}-ions tend to occupy the B-sites rather than the A-sites

in ABO_3- and A_2BO_4-type structures [26,27]. Additionally, as the TiO_2 content increases, the main peak intensities of the Sr_2TiO_4 phase gradually increases while the dominating peak intensity of the Sr_2CeO_4 phase gradually decreases due to the fact that some Ti^{4+}-ions directly replace Ce^{4+}-ions to generate Sr_2TiO_4 solid solutions. Based on this, it also indicates that the $x$$TiO_2$-(1 − x) ($SrCeO_3$ + Sr_2CeO_4) (x = 0.1–0.4) ceramic systems are a three-phase coexistence of the $SrCeO_3$ phase, the Sr_2CeO_4 phase and the Sr_2TiO_4 phase.

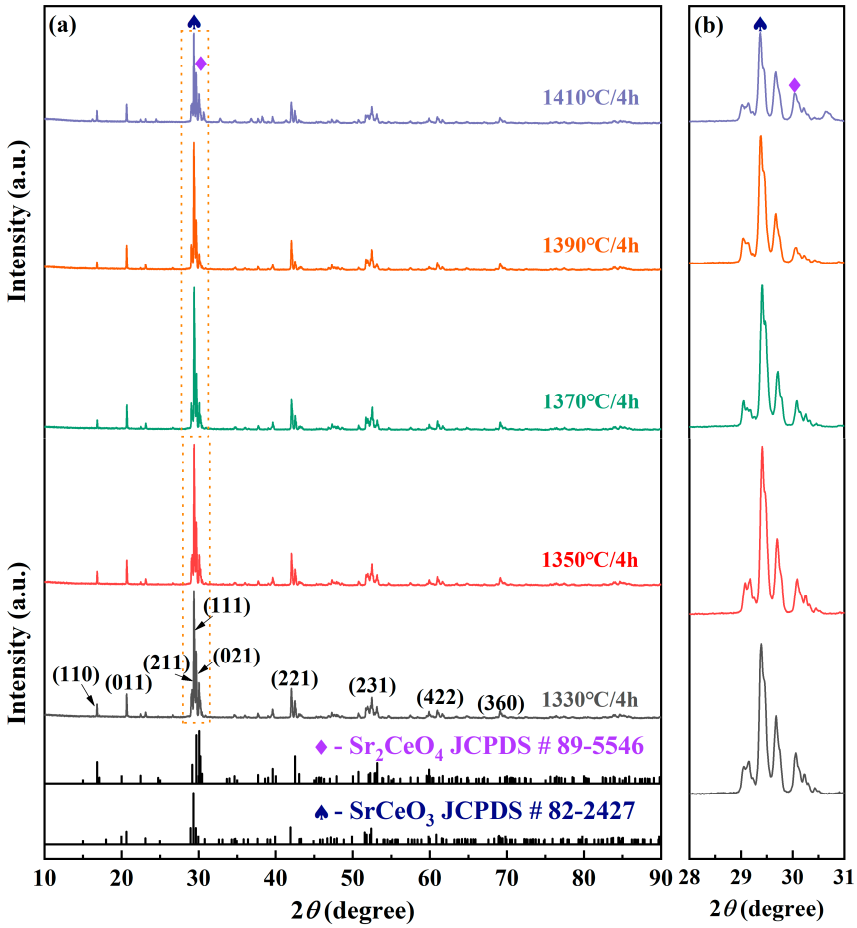

Figure 1. (**a**) Room-temperature XRD patterns of the (n + 1)SrO − $n$$CeO_2$ (n = 2) ceramics sintered at different temperatures for 4 h; (**b**) 2θ = 28–31° partially enlarged view.

Under normal conditions, Raman spectroscopy can be used to characterize phase transitions and explore crystal structures, due to its sensitivity to structural anomalies [28,29]. Figure 3a shows the room-temperature Raman spectra of the $x$$TiO_2$-(1 − x) ($SrCeO_3$ + Sr_2CeO_4) (x = 0.0–0.4) ceramics sintered at their optimum temperatures for 4 h in the range of 50–900 cm^{-1}. Based on the above XRD analysis modes, in order to more accurately judge the attribution of Raman peaks in these new composite ceramic systems, the Raman vibration modes of each pure phase structure with the $SrCeO_3$, Sr_2CeO_4 and Sr_2TiO_4 samples are provided here as the initial model for study. In this figure, the Raman peaks of the $x$$TiO_2$-(1 − x) ($SrCeO_3$ + Sr_2CeO_4) (x = 0.0–0.4) ceramic systems essentially contain all the vibrational modes of these three phases. The 14 main vibration mode regions (R_1–R_{14}) are marked in the diagram, and it should also be noted that other vibration modes are difficult to detect due to their weak intensity. In addition, it can be observed that the Raman modes of the pure matrix (x = 0.0) only change a little compared with the sintered samples (x = 0.1–0.4) doped with Ti^{4+}-ions as a whole. However, it is worth noting that a new peak R_{14} appears after doping with Ti^{4+}-ions when $x \geq 0.1$, and the intensity of R_{14} vibration modes gradually increases; the frequency band here should also be marked

as caused by O-Ti-O bending vibration [30]. Meanwhile, the intensity of the R_{13} vibration modes also gradually increases with the increase in TiO_2 content, and the Raman band at 500–650 cm^{-1} can be attributed to the Ti-O stretching vibration of the TiO_6 octahedron [31]. Both these two Raman modes belong to the Sr_2TiO_4 phase. Additionally, Figure 3b demonstrates that all the vibration modes of the main peak (R_7–R_{12}) are stable within the 287.17–386.21 cm^{-1} band range, and the Raman waveform of the main phase is still maintained within the Ti^{4+}-ions' doping range, which can explain that the frequency band here is related to the stretching vibration of CeO_6 octahedra [32]. In summary, the analysis results of Raman spectroscopy correspond to those of the XRD analysis, which further verifies the credibility and correctness of the phase compositions and structures of these $x TiO_2$-(1 − x) ($SrCeO_3$ + Sr_2CeO_4) (x = 0.0–0.4) ceramic systems.

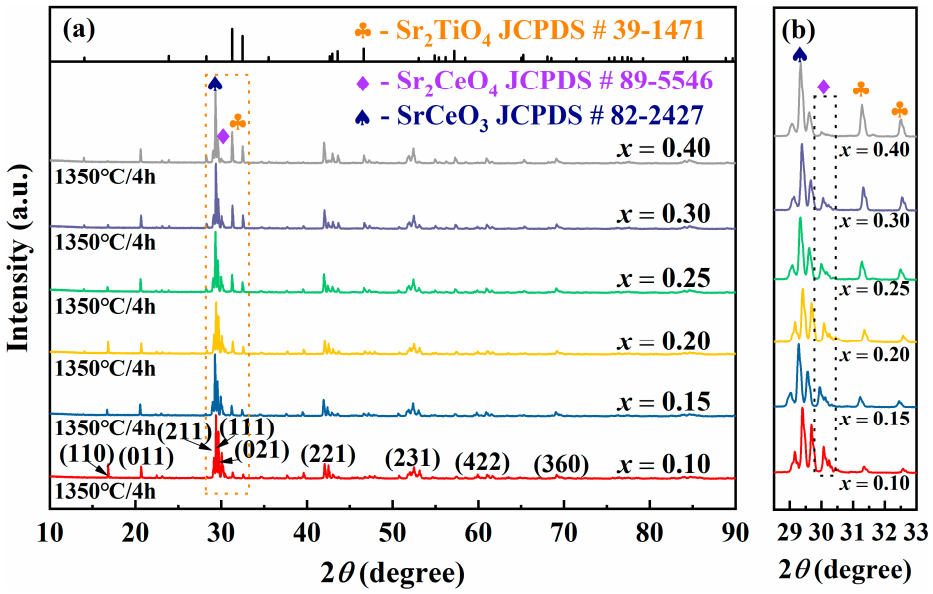

Figure 2. (**a**) Room temperature XRD patterns of the $x TiO_2$-(1 − x) ($SrCeO_3$ + Sr_2CeO_4) (x = 0.1–0.4) ceramics sintered at 1350 °C and (**b**) 2θ = 28.5–33° partially enlarged view.

In order to study the micro-morphology and structure of the sintered samples, SEM images were obtained from the surfaces of the $x TiO_2$-(1 − x) ($SrCeO_3$ + Sr_2CeO_4) (x = 0.0, 0.1, 0.15, 0.2, 0.25, 0.3, 0.4) ceramics, as shown in Figure 4. It can be clearly seen that all components basically form a comparatively dense ceramic matrix, and their grains are more evenly distributed and uniform. Additionally, only an extremely small amount of pores can be observed at the grain boundary, which is mainly caused by the part volatilization of Ce at the relatively high sintered temperatures [33,34]. From the illustrations in Figure 4a–g, it can be observed that the average grain size of Ti^{4+}-ion-doped samples is smaller compared with the pure matrix on the whole. All of the above phenomena confirm that the additional Ti^{4+}-ion content can not only affect the microscopic morphology, but can also influence grain growth to a large extent for ($SrCeO_3$ + Sr_2CeO_4)-based ceramic systems. It is worth noting that growth stripes have also been observed on some grains in similar research [35–37]. In conclusion, the two types of grains in the x = 0.0 matrix and three types of grains after doping with Ti^{4+}-ions can be observed in Figure 4a–g, indicating the formation of other phases, which is in good agreement with the results of the phase compositions in the XRD patterns and the Raman spectra analysis.

In order to further analyze the element composition and content of different grains, SEM images and EDS analysis data of the pure matrix $SrCeO_3$ + Sr_2CeO_4 ceramic sample sintered at 1350 °C for 4 h are shown in Figure 5. According to the above SEM analysis, two different types of grain regions (Region 1 and Region 2) can be observed in Figure 5a. The results of energy spectrum analysis in the gray grain area (Region 1) randomly selected

in Figure 5b show that the atomic percentage of Sr:Ce:O is approximately 1:1:3, which is consistent with the stoichiometry ratio of the $SrCeO_3$ phase. As shown in Figure 5c, the atomic ratio of Sr:Ce:O analyzed by EDS in the marked stripe grain area (Region 2) is about 2:1:4, which is close to the stoichiometric ratio of Sr_2CeO_4. Moreover, to further confirm the phase compositions and crystal structures, HRTEM (SEAD) pattern analysis was conducted on the pure matrix $SrCeO_3$ + Sr_2CeO_4 ceramic sample sintered at 1350 °C for 4 h. The TEM morphology images of the sample are shown in Figure 6a. The grain size of the pure matrix is about 2 μm, which is consistent with the grain size calculated from the SEM image. Figure 6b shows two different types of lattice stripes. The lattice stripe in "Region 1" has a crystalline spacing of 0.3022 nm corresponding to the (200) crystalline plane of the Sr_2CeO_4 phase, while "Region 2" has a crystalline spacing of 0.4256 nm, which corresponds to the (011) crystalline plane of the $SrCeO_3$ phase. This also indicates that both the $SrCeO_3$ and Sr_2CeO_4 phases exist in the x = 0.0 matrix sample, which is consistent with the XRD patterns, Raman spectra and SEM-EDS analysis results. The electron diffraction patterns, as shown in Figure 6c,d, also belong to the $SrCeO_3$ and Sr_2CeO_4 phases, which are attributed to the space group of Pmcn (62) and Pbam (55), respectively.

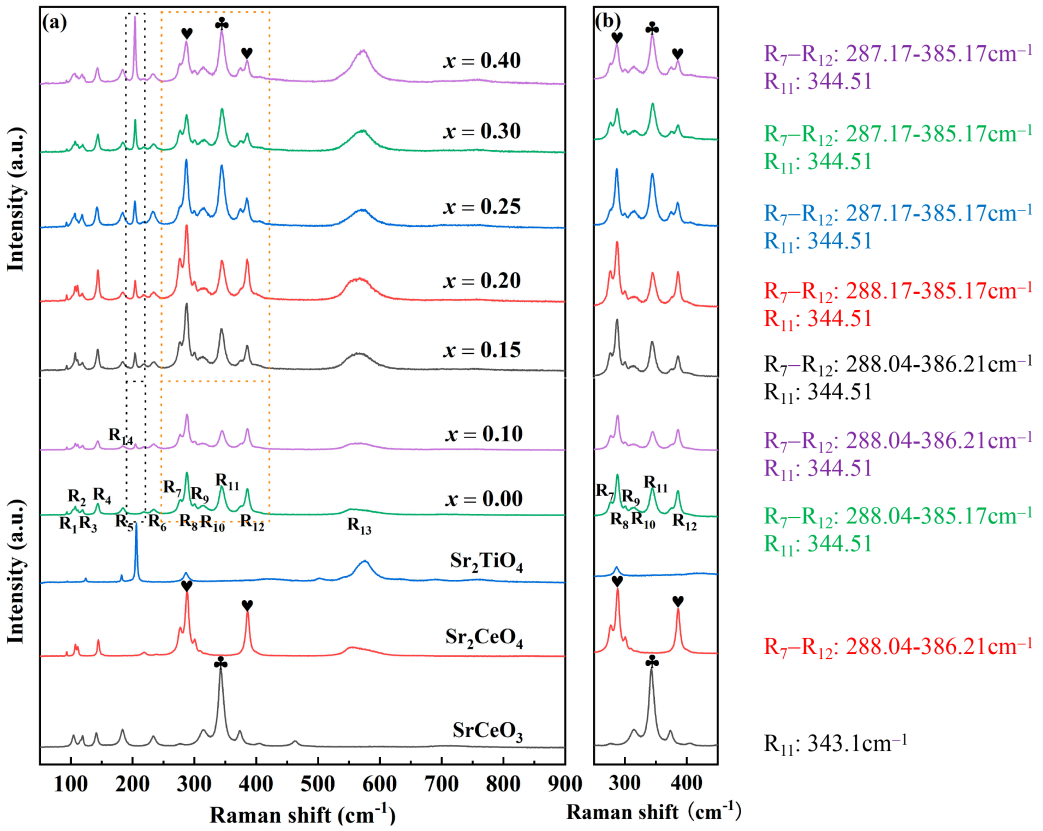

Figure 3. Raman spectra of $SrCeO_3$, Sr_2CeO_4, Sr_2TiO_4 and $x$$TiO_2$-(1 − x) ($SrCeO_3$ + Sr_2CeO_4) (x = 0.0–0.4) ceramics (**a**) in the range of 50–900 cm^{-1} and (**b**) in the range of 250–450 cm^{-1}, sintered at their optimal temperatures for 4 h.

In order to further explain the composition and content of the TiO_2-added samples, Figure 7 shows the surface morphology of $x$$TiO_2$-(1 − x) ($SrCeO_3$ + Sr_2CeO_4) (x = 0.2) ceramics along with the results of an energy-dispersive spectroscopy (EDS) analysis used to evaluate the grains of the sintered samples. As shown in Figure 7a, it can be clearly observed that the sintered samples are composed of these three different types of grains, which are identified as large grain areas (Region 1), striped grain areas (Region 2) and small grain areas (Region 3). The experimental atomic composition percentages of the large and striped grains are approximately 1:1:3 [Sr:(Ce + Ti):O = 22.38%:(20.54 + 0.23%):56.86%] and

2:1:4 [23.46%:(11.26 + 0.28%):64.99%], which are in general agreement with the theoretical values [Sr:(Ce + Ti):O = 20%:(19.6 + 0.4%):60%] and [28.57%:(13.86 + 0.43%):57.14%], respectively. Moreover, it is worth noting that the Ti content of these small grains is higher than that of the other two kinds of grains in Figure 7c. The elemental composition of these small grains is close to the stoichiometric ratio of Sr_2TiO_4. Eventually, the xTiO$_2$-(1 − x) ($SrCeO_3$ + Sr_2CeO_4) (x = 0.2) ceramics were confirmed to exist in $SrCeO_3$ and Sr_2CeO_4 as the main crystalline phases, and in Sr_2CeO_4 as the second phase.

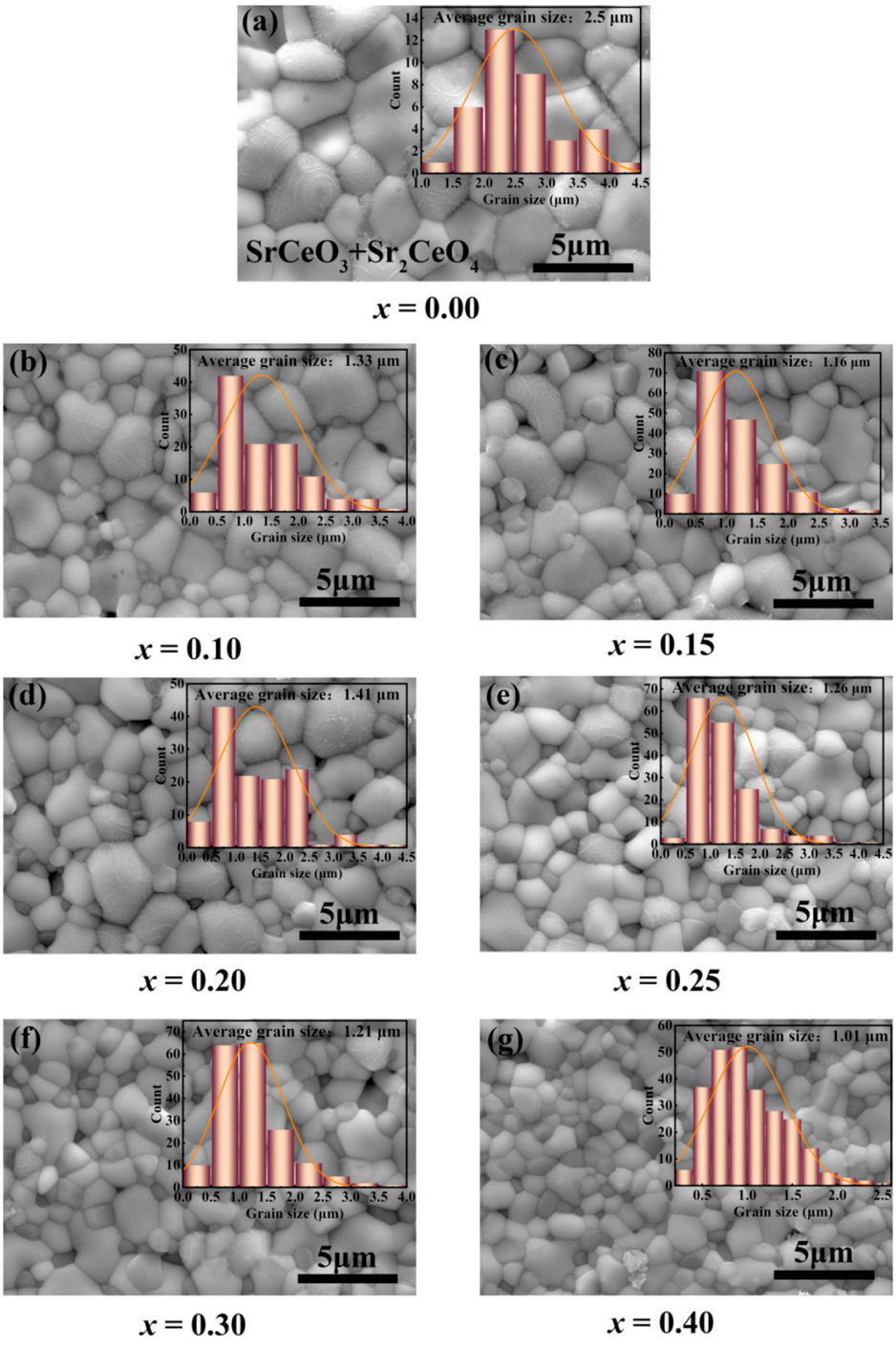

Figure 4. SEM images of the (**a**), (**b**), (**c**), (**d**), (**e**), (**f**) and (**g**) correspond to the xTiO$_2$-(1 − x) ($SrCeO_3$ + Sr_2CeO_4) (x = 0.0, 0.1, 0.15, 0.2, 0.25, 0.3, 0.4) ceramics sintered at their optimal temperatures for 4 h, respectively.

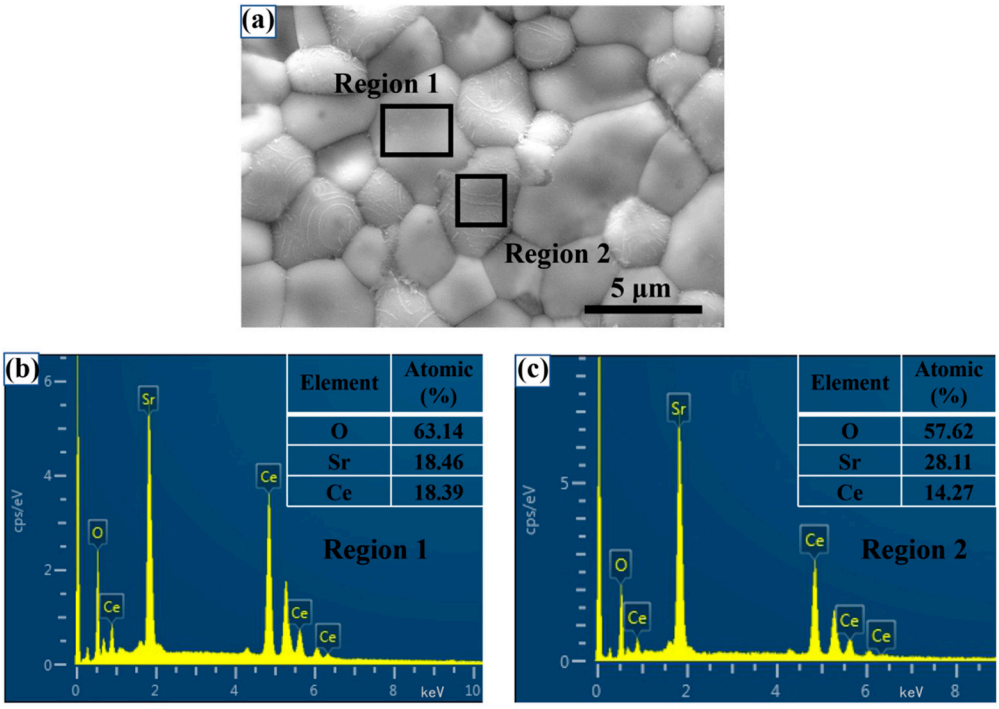

Figure 5. (**a**) SEM images (same as Figure 4a), (**b**,**c**) EDS spectra and data of the $SrCeO_3$ + Sr_2CeO_4 ceramic sample sintered at 1350 °C for 4 h.

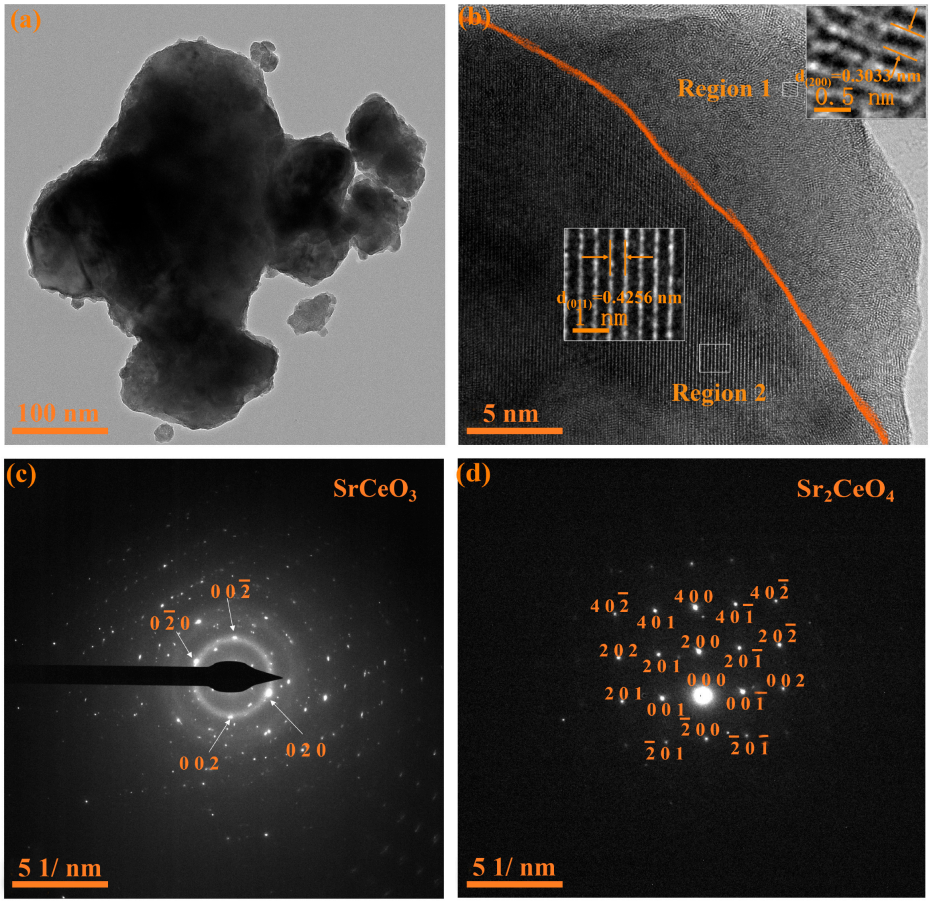

Figure 6. HRTEM images of the (**a**,**b**) $SrCeO_3$ + Sr_2CeO_4 ceramic sample; electron diffraction pictures of (**c**) $SrCeO_3$ and (**d**) Sr_2CeO_4 phases in this sintered sample at 1350 °C.

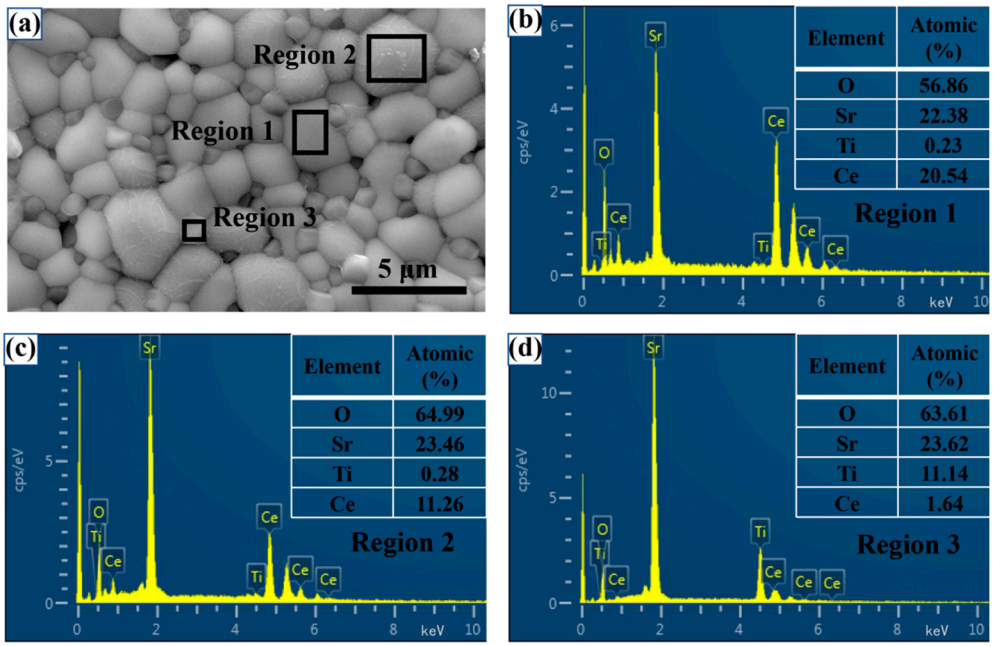

Figure 7. (**a**) SEM images (same as Figure 4d) and (**b**–**d**) EDS spectra and data of xTiO$_2$-(1-x) (SrCeO$_3$ + Sr$_2$CeO$_4$) (x = 0.2) ceramic samples sintered at 1350 °C for 4 h.

Figure 8 shows the changes in the bulk density and ε_r value of the xTiO$_2$-(1 − x) (SrCeO$_3$ + Sr$_2$CeO$_4$) (x = 0.0–0.4) ceramics as a function of TiO$_2$ content at their optimal temperatures. It can be observed that the variation in bulk density and ε_r values with different x values for the sintered samples follow almost the same increasing trend. Generally, the ε_r value is largely dependent on the compactness, phase content and quadratic equivalence [38–40]. In this work, the increase in bulk density means the higher compactness and the fewer defects were caused by extrinsic factors in these sintered specimens [41]. At the same time, the change in ε_r value after Ti^{4+}-ion doping should be partly attributed to the increasing content of the secondary phase Sr$_2$TiO$_4$ with a higher ε_r value (~42) before the samples of $x \leq 0.2$ [18]. Finally, the ε_r value of the composite phase ceramics is also determined by the combination of the constituent materials with different volume fractions, and it is also most likely to be related to the higher ε_r value (~104) of the TiO$_2$-added material [42,43]. Therefore, after comprehensive evaluation, the variation tendency of the ε_r value is expected in these xTiO$_2$-(1 − x) (SrCeO$_3$ + Sr$_2$CeO$_4$) (x = 0.0–0.4) composite phase ceramic systems as described in Figure 8b.

Usually, complex impedance spectroscopy is an efficient method by which to investigate the conductive behavior of materials, in particular, the different conductive properties of grains, grain boundaries and interfaces in polycrystalline bulk ceramic materials [44]. The complex impedance plots of the SrCeO$_3$ + Sr$_2$CeO$_4$ and xTiO$_2$-(1 − x) (SrCeO$_3$ + Sr$_2$CeO$_4$) (x = 0.2) samples sintered at their optimal temperatures for 4 h and tested at 180–360 °C in the frequency range of 100 Hz–1 MHz are shown in Figure 9a,c, respectively. The impedance real part is represented by the x-axis (Z'), and the impedance imaginary part is represented by the y-axis (Z''). The conductivity of the SrCeO$_3$ + Sr$_2$CeO$_4$ and xTiO$_2$-(1 − x) (SrCeO$_3$ + Sr$_2$CeO$_4$) (x = 0.2) samples increases with temperature; the intercept on the x-axis demonstrates a negative temperature effect, similar to that of semiconductor resistance [45]. It is worth noting that, as the temperature increases, two semicircular arcs with different radii appear in the measured samples from the grain boundary response in the low-frequency region and the grain contribution in the high-frequency region. This phenomenon is due to the different time response constants of grains and grain boundaries, and it also reflects their structural differences [46]. The experimental data were fitted based on the equivalent circuit diagrams, using the Zview software to better separate the different conductive contributions of grains and grain boundaries, as shown

in Figure 9a,c. The circuit consists of two series-connected resistor constant-phase components, where R_g represents grain resistance and R_{gb} represents grain boundary resistance. The Arrhenius relationships for the grains and grain boundaries of the $SrCeO_3$ + Sr_2CeO_4 and $x$$TiO_2$-(1 − x) ($SrCeO_3$ + Sr_2CeO_4) (x = 0.2) samples are shown in Figure 9b,d. The activation energy required for thermally activated conduction can be estimated by fitting the data to the Arrhenius formula [47]:

$$\sigma = \sigma_p \exp\left(-\frac{E_a}{KT}\right) \quad (2)$$

where σ_p is the pre-exponential factor of conduction, σ_p is the activation energy required for conduction, K is the Boltzmann constant and T is the temperature in Kelvin. The results obtained from the fitting calculations show that the activation energies of the grains and grain boundaries of the $SrCeO_3$ + Sr_2CeO_4 and $x$$TiO_2$-(1 − x) ($SrCeO_3$ + Sr_2CeO_4) (x = 0.2) samples are 0.33 eV, 0.37 eV, 0.31 eV and 0.34 eV, respectively. This suggests that the conduction type of the $SrCeO_3$ + Sr_2CeO_4 and $x$$TiO_2$-(1 − x) ($SrCeO_3$ + Sr_2CeO_4) (x = 0.2) samples sintered at higher temperatures is single ionized oxygen vacancies [48]. In addition, the x = 0.2 sample has a lower activation energy than the pure matrix; in other words, the doped sample possess a larger resistance. The large resistance of the x = 0.2 sample is a result of grain refinement and the creation of the second phase, which increases the grain boundaries and thus impedes the movement of carriers, and also balances the fluctuations caused by thermal fluctuations. In summary, the $x$$TiO_2$-(1 − x) ($SrCeO_3$ + Sr_2CeO_4) (x = 0.2) sample has the better temperature stability.

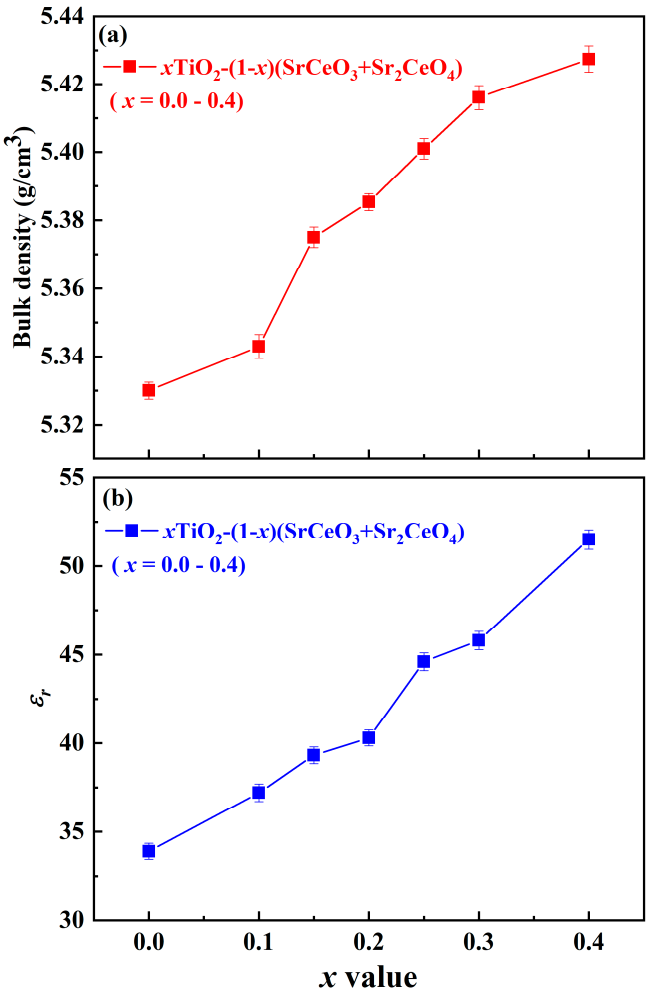

Figure 8. (**a**) Bulk density and (**b**) ε_r of the $x$$TiO_2$-(1 − x) ($SrCeO_3$ + Sr_2CeO_4) (x = 0.0–0.4) ceramics sintered at their optimal temperatures for 4 h.

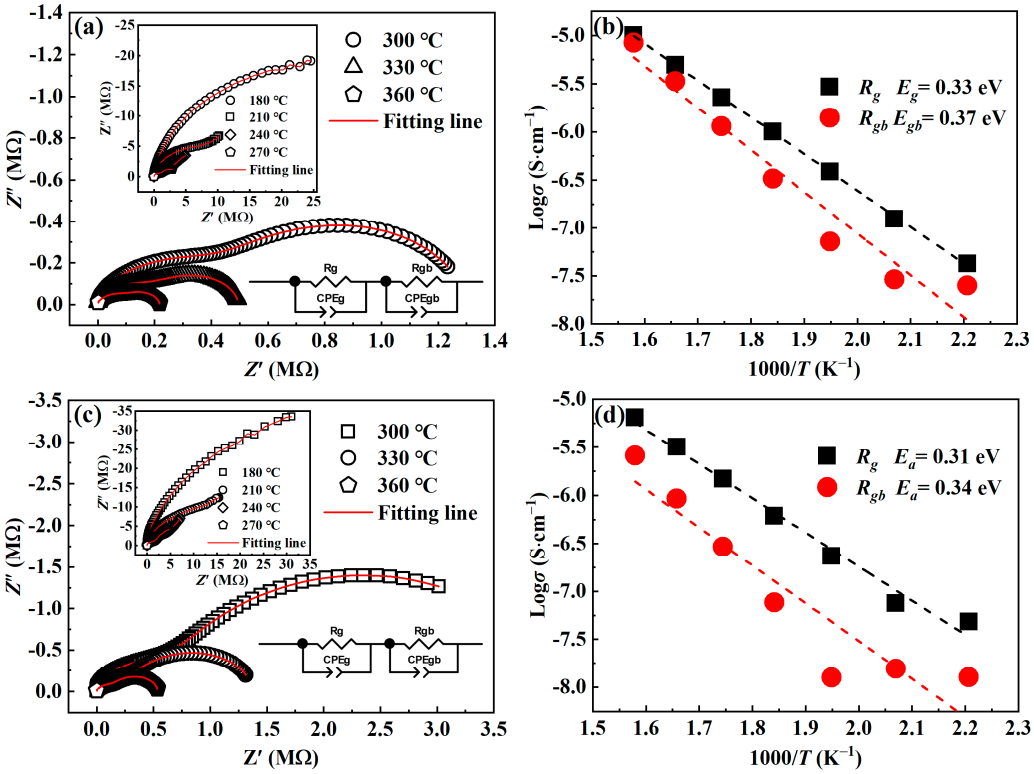

Figure 9. Complex impedance diagrams, equivalent circuit diagrams and activation energy diagrams of (**a**,**b**) the $SrCeO_3$ + Sr_2CeO_4 and (**c**,**d**) the $x$$TiO_2$-(1 − x) ($SrCeO_3$ + Sr_2CeO_4) (x = 0.2) ceramics sintered at their optimal temperatures for 4 h.

Figure 10 shows the $Q \times f$ and τ_f values of the $x$$TiO_2$-(1 − x) ($SrCeO_3$ + Sr_2CeO_4) (x = 0.0–0.4) ceramics sintered at their optimal temperatures for 4 h, and Table 1 also includes the detailed data of f_0, ε_r, $Q \times f$ and tan δ for the different component ceramic systems at different sintering temperatures. Combining the test data in Table 1 and Figure 10, it can be observed that the x = 0.0 sample sintered at 1350 °C has the better microwave dielectric properties, and the ε_r, $Q \times f$ and τ_f values are 33.9, 41,090 GHz (at 7.21 GHz) and −46.6 ppm/°C, respectively. In addition, the values of ε_r and τ_f of the $x$$TiO_2$-(1 − x) ($SrCeO_3$ + Sr_2CeO_4) (x = 0.1–0.4) ceramics increase linearly from 37.2 and −26.4 ppm/°C to 51.5 and + 45.4 ppm/°C, respectively. In particular, when x = 0.2, a near-zero τ_f value of −4.6 ppm/°C can be acquired. The $Q \times f$ value first increases from 42,350 GHz (at 6.86 GHz) with the x = 0.1 sample sintered at 1350 °C to 44,020 GHz (at 6.56 GHz) with the x = 0.2 sample sintered at 1330 °C, and then decreases linearly to 39,700 GHz (at 5.68 GHz) with the x = 0.4 sample sintered at 1350 °C. It can also be seen from the Q value data that the overall range of change is not very large in these investigated x values. The relationship between quality factor and dielectric loss is usually negatively correlated. When x = 0.2, the $Q \times f$ value reaches its maximum value, and the average grain size of this component is the largest among all the doped components (x = 0.1–0.4), which is in good agreement with the calculations in Figure 4. In general, a larger grain size and fewer grain boundaries will give rise to a smaller dielectric loss. Therefore, the grain size is also one of the main reasons for improving the $Q \times f$ value of these sintered samples [49,50]. The influence of quality factors is often attributed to the impurities and other equivalent external factors, and the external factors are a common discussion point at present. Thus, in order to obtain the optimum $Q \times f$ value, the best combination of the external factors including its grain size, secondary phase and porosity should be considered as a whole [51,52]. In summary, the addition of Ti^{4+}-ions plays a good complementary role to the microwave dielectric properties of the $x$$TiO_2$-(1 − x) ($SrCeO_3$ + Sr_2CeO_4) (x = 0.0–0.4) ceramic systems.

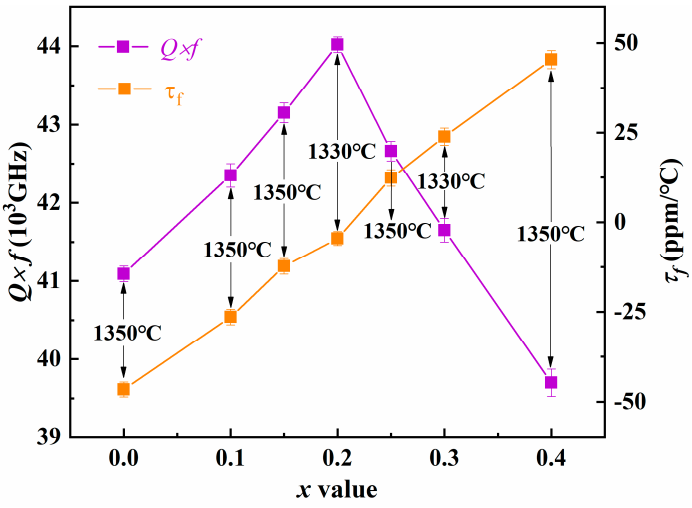

Figure 10. $Q \times f$ and τ_f values for the xTiO$_2$-(1 − x) (SrCeO$_3$ + Sr$_2$CeO$_4$) (x = 0.0–0.4) ceramics sintered at their optimal temperatures for 4 h.

Table 1. Sintering temperature, f_0, ε_r, $Q \times f$ and tan δ values of the xTiO$_2$-(1 − x) (SrCeO$_3$ + Sr$_2$CeO$_4$) (x = 0.0–0.4) specimens at different sintering temperatures for 4 h.

Compounds	Sintering Temperature (°C)	f_0 (GHz)	ε_r	$Q \times f$ (GHz)	Tan δ
x = 0.0	1330	7.27	32.1	40,200	0.000182
x = 0.0	1350	7.21	33.9	41,090	0.000181
x = 0.0	1370	7.17	33.9	39,810	0.000180
x = 0.0	1390	7.20	33.9	39,980	0.000180
x = 0.0	1410	7.23	33.2	40,060	0.000176
x = 0.1	1310	6.94	35.8	39,440	0.000176
x = 0.1	1330	6.88	36.8	40,950	0.000168
x = 0.1	1350	6.86	37.2	42,350	0.000163
x = 0.1	1370	6.85	37.1	42,310	0.000162
x = 0.1	1390	6.84	37.2	41,230	0.000166
x = 0.15	1310	6.83	35.9	26,280	0.000217
x = 0.15	1330	6.69	38.5	38,800	0.000152
x = 0.15	1350	6.65	39.3	43,150	0.000154
x = 0.15	1370	6.60	40.2	42,880	0.000154
x = 0.15	1390	6.59	40.3	42,240	0.000156
x = 0.2	1310	6.63	38.7	35,670	0.000186
x = 0.2	1330	6.56	40.3	44,020	0.000152
x = 0.2	1350	6.53	40.4	37,330	0.000175
x = 0.2	1370	6.52	40.9	38,330	0.000170
x = 0.2	1390	6.51	41.2	37,640	0.000174
x = 0.25	1310	6.33	41.7	40,360	0.000158
x = 0.25	1330	6.25	43.9	41,110	0.000152
x = 0.25	1350	6.21	44.6	42,660	0.000149
x = 0.25	1370	6.20	43.9	40,280	0.000155
x = 0.25	1390	6.19	45.2	40,440	0.000154
x = 0.3	1310	6.17	43.1	36,140	0.000171
x = 0.3	1330	6.08	45.8	41,650	0.000146
x = 0.3	1350	6.04	46.6	40,830	0.000149
x = 0.3	1370	6.01	47.3	41,190	0.000147
x = 0.3	1390	6.01	47.5	40,590	0.000149
x = 0.4	1310	5.79	48.6	36,860	0.000158
x = 0.4	1330	5.70	51.0	39,040	0.000147
x = 0.4	1350	5.68	51.5	39,700	0.000144
x = 0.4	1370	5.67	51.7	39,080	0.000146
x = 0.4	1390	5.66	51.8	38,530	0.000147

4. Conclusions

The $(n + 1)SrO - nCeO_2$ ($n = 2$) and $xTiO_2$-$(1 - x)$ $(SrCeO_3 + Sr_2CeO_4)$ ($x = 0.1$–0.4) ceramic systems were successfully synthesized using the solid-state reaction method. The results of XRD pattern analysis showed that the $(n + 1)SrO - nCeO_2$ ($n = 2$) ceramic system prepared with the solid-phase reaction method did not form a solid solution, showing a composite phase system with the coexistence of $SrCeO_3$ and Sr_2CeO_4 phases, which belonged to the orthogonal structures with the different space groups of the Pmcn(62) and Pbam(55), respectively. For the $xTiO_2$-$(1 - x)$ $(SrCeO_3 + Sr_2CeO_4)$ ($x = 0.1$–0.4) ceramic samples, a second phase of Sr_2TiO_4 started to occur as $x \geq 0.1$, and with the increase in x value, the content of the second phase increased as well. In addition, the phase compositions and crystal structures of the given ceramic systems were further verified by Raman spectroscopy, EDS spectroscopy and HRTEM (SAED) detection. Moreover, complex impedance spectroscopy was used to analyze the conductivity behavior of composite ceramic systems with different Ti^{4+}-ion doping content. The results showed that the moderate doping of Ti^{4+}-ions could indeed promote the thermal stability of these ceramic samples to some extent. Among them, the $xTiO_2$-$(1 - x)$ $(SrCeO_3 + Sr_2CeO_4)$ ($x = 0.2$) ceramic system sintered at 1330 °C for 4 h possessed the better comprehensive microwave dielectric properties: $\varepsilon_r = 40.3$, $Q \times f = 44{,}020$ GHz (at 6.56 GHz) and $\tau_f = -4.6$ ppm/°C. This is expected to be a new candidate material for key components of filters.

Author Contributions: Q.S.: Investigation, Writing—Original draft preparation, Data Curation. J.Q.: Software, Methodology. F.L.: Conceptualization, Methodology, Writing—Review and Editing. C.Y.: Writing—Review and Editing. X.L.: Validation. M.S.: Writing—Review and Editing, Resources. L.M.: Validation. G.C.: Resources, Supervision. All authors have read and agreed to the published version of the manuscript.

Funding: The financial support of the National Natural Science Foundation of China (Grant No.12264009), the Natural Science Foundation of Guangxi Province, China Grant Nos. 2023GXNSFAA026513 and 2020GXNSFBA159027), and the Guangxi Key Laboratory of Manufacturing System & Advanced Manufacturing Technology (Grant No. 20-065-40-001z) are gratefully acknowledged by the authors.

Data Availability Statement: All data generated or analyzed during this study are included in this published article.

Conflicts of Interest: The authors declare that they have no conflict of interest.

References

1. Zhou, D.; Pang, L.X.; Wang, D.W.; Reaney, I.M. $BiVO_4$ Based High: K Microwave Dielectric Materials: A Review. *J. Mater. Chem. C Mater.* **2018**, *6*, 9290–9313. [CrossRef]
2. Zhou, D.; Pang, L.X.; Wang, D.W.; Li, C.; Jin, B.B.; Reaney, I.M. High Permittivity and Low Loss Microwave Dielectrics Suitable for 5G Resonators and Low Temperature Co-Fired Ceramic Architecture. *J. Mater. Chem. C Mater.* **2017**, *5*, 10094–10098. [CrossRef]
3. Green, M.; Chen, X. Recent Progress of Nanomaterials for Microwave Absorption. *J. Mater.* **2019**, *5*, 503–541. [CrossRef]
4. Green, M.; Xiang, P.; Liu, Z.; Murowchick, J.; Tan, X.; Huang, F.; Chen, X. Microwave Absorption of Aluminum/Hydrogen Treated Titanium Dioxide Nanoparticles. *J. Mater.* **2019**, *5*, 133–146. [CrossRef]
5. Trukhanov, A.; Astapovich, K.A.; Turchenko, V.A.; Almessiere, M.A.; Slimani, Y.; Baykal, A.; Sombra, A.S.B.; Zhou, D.; Jotania, R.B.; Singh, C.; et al. Influence of the Dysprosium Ions on Structure, Magnetic Characteristics and Origin of the Reflection Losses in the Ni-Co Spinels. *J. Alloys Compd.* **2020**, *841*, 155667. [CrossRef]
6. Klygach, D.S.; Vakhitov, M.G.; Vinnik, D.A.; Bezborodov, A.; Gudkova, S.A.; Zhivulin, V.E.; Zherebtsov, D.A.; SakthiDharan, C.P.; Trukhanov, S.; Trukhanov, A.; et al. Measurement of Permittivity and Permeability of Barium Hexaferrite. *J. Magn. Magn. Mater.* **2018**, *465*, 290–294. [CrossRef]
7. Liu, B.; Huang, Y.H.; Song, K.X.; Li, L.; Chen, X.M. Structural Evolution and Microwave Dielectric Properties in $Sr_2(Ti_{1-x}Sn_x)O_4$ Ceramics. *J. Eur. Ceram. Soc.* **2018**, *38*, 3833–3839. [CrossRef]
8. Algarou, N.A.; Slimani, Y.; Almessiere, M.A.; Sadaqat, A.; Trukhanov, A.; Gondal, M.A.; Hakeem, A.S.; Trukhanov, S.; Vakhitov, M.G.; Klygach, D.S.; et al. Functional $Sr_{0.5}ba_{0.5}Sm_{0.02}Fe_{11.98}O_{4/x}(Ni_{0.8}Zn_{0.2}Fe_2O_4)$ Hard-Soft Ferrite Nanocomposites: Structure, Magnetic and Microwave Properties. *Nanomaterials* **2020**, *10*, 2134. [CrossRef]
9. Hao, S.Z.; Zhou, D.; Hussain, F.; Liu, W.F.; Su, J.Z.; Wang, D.W.; Wang, Q.P.; Qi, Z.M.; Singh, C.; Trukhanov, S. Structure, Spectral Analysis and Microwave Dielectric Properties of Novel $x(NaBi)_{0.5}MoO_4$-$(1 - x)Bi_{2/3}MoO_4$ ($x = 0.2$~0.8) Ceramics with Low Sintering Temperatures. *J. Eur. Ceram. Soc.* **2020**, *40*, 3569–3576. [CrossRef]

10. Guo, H.H.; Zhou, D.; Du, C.; Wang, P.J.; Liu, W.F.; Pang, L.X.; Wang, Q.P.; Su, J.Z.; Singh, C.; Trukhanov, S. Temperature Stable $Li_2Ti_{0.75}(Mg_{1/3}Nb_{2/3})_{0.25}O_3$-Based Microwave Dielectric Ceramics with Low Sintering Temperature and Ultra-Low Dielectric Loss for Dielectric Resonator Antenna Applications. *J. Mater. Chem. C Mater.* **2020**, *8*, 4690–4700. [CrossRef]
11. Liu, B.; Hu, C.C.; Huang, Y.H.; Song, K.X. Effects of $(Mg_{1/3}Nb_{2/3})$ Substitution on the Structure and Microwave Dielectric Properties of Sr_2TiO_4 Ceramics. *Mater. Lett.* **2019**, *253*, 293–297. [CrossRef]
12. Song, X.Q.; Lu, W.Z.; Wang, X.C.; Wang, X.H.; Fan, G.F.; Muhammad, R.; Lei, W. Sintering Behaviour and Microwave Dielectric Properties of $BaAl_{2-2x}(ZnSi)_xSi_2O_8$ Ceramics. *J. Eur. Ceram. Soc.* **2018**, *38*, 1529–1534. [CrossRef]
13. Induja, I.J.; Sebastian, M.T. Microwave Dielectric Properties of Mineral Sillimanite Obtained by Conventional and Cold Sintering Process. *J. Eur. Ceram. Soc.* **2017**, *37*, 2143–2147. [CrossRef]
14. Song, X.Q.; Lu, W.Z.; Lou, Y.H.; Chen, T.; Ta, S.W.; Fu, Z.X.; Lei, W. Synthesis, Lattice Energy and Microwave Dielectric Properties of $BaCu_{2-x}Co_xSi_2O_7$ Ceramics. *J. Eur. Ceram. Soc.* **2020**, *40*, 3035–3041. [CrossRef]
15. Ohsato, H.; Tsunooka, T.; Sugiyama, T.; Kakimoto, K.I.; Ogawa, H. Forsterite Ceramics for Millimeterwave Dielectrics. *J. Electroceram.* **2006**, *17*, 445–450. [CrossRef]
16. Su, C.; Ao, L.; Zhang, Z.; Zhai, Y.; Chen, J.; Tang, Y.; Liu, L.; Fang, L. Crystal Structure, Raman Spectra and Microwave Dielectric Properties of Novel Temperature-Stable $LiYbSiO_4$ Ceramics. *Ceram. Int.* **2020**, *46*, 19996–20003. [CrossRef]
17. Su, Q.; Qu, J.J.; Liu, F.; Feng, A.L.; Yuan, C.L.; Liu, X.; Meng, L.F.; Ding, G.A.; Su, M.W.; Chen, G.H. Dielectric Properties of Ti^{4+}/Zr^{4+} Modified the $SrCeO_3$-Based Microwave Ceramic Systems. *J. Mater. Sci. Mater. Electron.* **2023**, *34*, 156. [CrossRef]
18. Dai, Q.; Zuo, R. A Novel Ultralow-Loss Sr_2CeO_4 Microwave Dielectric Ceramic and Its Property Modification. *J. Eur. Ceram. Soc.* **2019**, *39*, 1132–1136. [CrossRef]
19. Hakki, B.W.; Coleman, P.D. A Dielectric Resonator Method of Measuring Inductive Capacities in the Millimeter Range. *IEEE Trans. Microw. Theory Tech.* **1960**, *8*, 402–410. [CrossRef]
20. Rajput, S.S.; Keshri, S.; Gupta, V.R. Microwave Dielectric Properties of $(1-x)Mg_{0.95}Zn_{0.05}TiO_3$-$(x)Ca_{0.6}La_{0.8/3}TiO_3$ Ceramic Composites. *J. Alloys Compd.* **2013**, *552*, 219–226. [CrossRef]
21. Kim, E.S.; Yoon, K.H. Microwave Dielectric Properties of $(1-x)CaTiO_3$-$xLi_{1/2}Sm_{1/2}TiO_3$ Ceramics. *J. Eur. Ceram. Soc.* **2003**, *23*, 2397–2401. [CrossRef]
22. Wang, T.; Wang, X.L.; Song, S.H.; Ma, Q. Effect of Rare-Earth Nd/Sm Doping on the Structural and Multiferroic Properties of $BiFeO_3$ Ceramics Prepared by Spark Plasma Sintering. *Ceram. Int.* **2020**, *46*, 15228–15235. [CrossRef]
23. Ren, Z.; Zhang, N.; Long, X.; Ye, Z.G. New Antiferroelectric Solid Solution of $(Mg_{1/2}W_{1/2})O_3$-$Pb(Zn_{1/2}W_{1/2})O_3$ as Dielectric Ceramics. *J. Am. Ceram. Soc.* **2014**, *97*, 1700–1703. [CrossRef]
24. Ahmad, T.; Ganguli, A.K. Reverse Micellar Route to Nanocrystalline Titanates ($SrTiO_3$, Sr_2TiO_4, and $PbTiO_3$): Structural Aspects and Dielectric Properties. *J. Am. Ceram. Soc.* **2006**, *89*, 1326–1332. [CrossRef]
25. Mao, M.M.; Chen, X.M.; Liu, X.Q. Structure and Microwave Dielectric Properties of Solid Solution in $SrLaAlO_4$-Sr_2TiO_4 System. *J. Am. Ceram. Soc.* **2011**, *94*, 3948–3952. [CrossRef]
26. Shannon, R.D. Revised Effective Ionic Radii and Systematic Studies of Interatomic Distances in Halides and Chalcogenides. *Acta Crystallogr. Sect. A* **1976**, *32*, 751–767. [CrossRef]
27. Ichinose, N.; Mutoh, K. Microwave Dielectric Properties in the $(1-x)$ $(Na_{1/2}La_{1/2})TiO_3$–$x(Li_{1/2}Sm_{1/2})TiO_3$ Ceramic System. *J. Eur. Ceram. Soc.* **2003**, *23*, 2455–2459. [CrossRef]
28. Lan, X.K.; Li, J.; Zou, Z.Y.; Xie, M.Q.; Fan, G.F.; Lu, W.Z.; Lei, W. Improved Sinterability and Microwave Dielectric Properties of $[Zn_{0.5}Ti_{0.5}]^{3+}$-doped $ZnAl_2O_4$ Spinel Solid Solution. *J. Am. Ceram. Soc.* **2019**, *102*, 5952–5957. [CrossRef]
29. Li, H.; Chen, X.; Xiang, Q.; Tang, B.; Lu, J.; Zou, Y.; Zhang, S. Structure, Bond Characteristics and Raman Spectra of $CaMg_{1-x}Mn_xSi_2O_6$ Microwave Dielectric Ceramics. *Ceram. Int.* **2019**, *45*, 14160–14166. [CrossRef]
30. Pinatti, I.M.; Mazzo, T.M.; Gonçalves, R.F.; Varela, J.A.; Longo, E.; Rosa, I.L.V. $CaTiO_3$ and $Ca_{1-3x}Sm_xTiO_3$: Photoluminescence and Morphology as a Result of Hydrothermal Microwave Methodology. *Ceram. Int.* **2016**, *42*, 1352–1360. [CrossRef]
31. Qu, J.; Liu, F.; Wei, X.; Yuan, C.; Liu, X.; Chen, G.; Feng, Q. X-ray Diffraction, Dielectric, and Raman Spectroscopy Studies of $SrTiO_3$-Based Microwave Ceramics. *J. Electron. Mater.* **2016**, *45*, 715–721. [CrossRef]
32. Scherban, T.; Villeneuve, R.; Abello, L.; Lucazeau, G. Raman Scattering Study of $BaCeO_3$ and $SrCeO_3$. *Solid State Commun.* **1992**, *84*, 341–344. [CrossRef]
33. Zhou, C.; Chen, G.; Cen, Z.; Yuan, C.; Yang, Y.; Li, W. Structure and Microwave Dielectric Characteristics of Lithium-Excess $Ca_{0.6}Nd_{0.8/3}TiO_3/(Li_{0.5}Nd_{0.5})TiO_3$ Ceramics. *Mater. Res. Bull.* **2013**, *48*, 4924–4929. [CrossRef]
34. Zhang, C.; Lu, L.; Yang, D. Preparation and Positive Temperature Coefficient of Resistivity Behavior of $BaTiO_3$-$BaBiO_3$-$Bi_{0.5}Na_{0.5}TiO_3$ Ceramics. *J. Mater. Sci. Mater. Electron.* **2015**, *26*, 8193–8198. [CrossRef]
35. Fu, M.S.; Liu, X.Q.; Chen, X.M. Structure and Microwave Dielectric Characteristics of $Ca_{1-x}Nd_{2x/3}TiO_3$ Ceramics. *J. Eur. Ceram. Soc.* **2008**, *28*, 585–590. [CrossRef]
36. Huang, C.-L.; Tsai, J.-T.; Chen, Y.-B. Dielectric Properties of $(1-y)Ca_{1-x}La2_{x/3}TiO_3 - y(Li, Nd)_{1/2}TiO_3$ Ceramic System at Microwave Frequency. *Mater. Res. Bull.* **2001**, *36*, 547–556. [CrossRef]
37. Ullah, B.; Lei, W.; Zou, Z.Y.; Wang, X.H.; Lu, W.Z. Synthesis Strategy, Phase-Chemical Structure and Microwave Dielectric Properties of Paraelectric $Sr_{(1-3x/2)}Ce_xTiO_3$ ceramics. *J. Alloys Compd.* **2017**, *695*, 648–655. [CrossRef]
38. Kim, E.S.; Chun, B.S.; Kang, D.H. Effects of Structural Characteristics on Microwave Dielectric Properties of $(1-x)Ca_{0.85}Nd_{0.1}TiO_3 - xLnAlO_3$ (Ln = Sm, Er and Dy) Ceramics. *J. Eur. Ceram. Soc.* **2007**, *27*, 3005–3010. [CrossRef]

39. Lan, X.K.; Li, J.; Zou, Z.Y.; Fan, G.F.; Lu, W.Z.; Lei, W. Lattice Structure Analysis and Optimised Microwave Dielectric Properties of $LiAl_{1-x}(Zn_{0.5}Si_{0.5})_xO_2$ Solid Solutions. *J. Eur. Ceram. Soc.* **2019**, *39*, 2360–2364. [CrossRef]
40. Liu, F.; Yuan, C.; Liu, X.; Qu, J.; Chen, G.; Zhou, C. Effects of Structural Characteristics on Microwave Dielectric Properties of $(Sr_{0.2}Ca_{0.488}Nd_{0.208})Ti_{1-x}Ga_{4x/3}O_3$ Ceramics. *Mater. Res. Bull.* **2015**, *70*, 678–683. [CrossRef]
41. Chen, X.; Li, H.; Zhang, P.; Hu, H.; Tao, Y.; Li, G. $SrZnV_2O_7$: A Low-Firing Microwave Dielectric Ceramic with High-Quality Factor. *J. Am. Ceram. Soc.* **2021**, *104*, 5110–5119. [CrossRef]
42. Guo, J.; Zhou, D.; Zou, S.L.; Wang, H.; Pang, L.X.; Yao, X. Microwave Dielectric Ceramics Li_2MO_4-TiO_2 (M = Mo, W) with Low Sintering Temperatures. *J. Am. Ceram. Soc.* **2014**, *97*, 1819–1822. [CrossRef]
43. Alford, N.M.; Breeze, J.; Wang, X.; Penn, S.J.; Dalla, S.; Webb, S.J.; Ljepojevic, N.; Aupi, X. Dielectric Loss of Oxide Single Crystals and Polycrystalline Analogues from 10 to 320 K. *J. Eur. Ceram. Soc.* **2001**, *21*, 2605–2611. [CrossRef]
44. Behera, B.; Nayak, P.; Choudhary, R.N.P. Impedance Spectroscopy Study of $NaBa_2V_5O_{15}$ Ceramic. *J. Alloys Compd.* **2007**, *436*, 226–232. [CrossRef]
45. Lily, K.; Kumari, K.; Prasad, K.; Choudhary, R.N.P. Impedance Spectroscopy of $(Na_{0.5}Bi_{0.5})$ $(Zr_{0.25}Ti_{0.75})O_3$ Lead-Free Ceramic. *J. Alloys Compd.* **2008**, *453*, 325–331. [CrossRef]
46. Barick, B.K.; Mishra, K.K.; Arora, A.K.; Choudhary, R.N.P.; Pradhan, D.K. Impedance and Raman Spectroscopic Studies of $(Na_{0.5}Bi_{0.5})TiO_3$. *J. Phys. D Appl. Phys.* **2011**, *44*, 355402. [CrossRef]
47. Christie, G. Microstructure—Ionic Conductivity Relationships in Ceria-Gadolinia Electrolytes. *Solid State Ion.* **1996**, *83*, 17–27. [CrossRef]
48. Liu, L.; Huang, Y.; Su, C.; Fang, L.; Wu, M.; Hu, C.; Fan, H. Space-Charge Relaxation and Electrical Conduction in $K_{0.5}Na_{0.5}NbO_3$ at High Temperatures. *Appl. Phys. A Mater. Sci. Process.* **2011**, *104*, 1047–1051. [CrossRef]
49. Green, M.; Liu, Z.; Xiang, P.; Liu, Y.; Zhou, M.; Tan, X.; Huang, F.; Liu, L.; Chen, X. Doped, Conductive SiO_2 Nanoparticles for Large Microwave Absorption. *Light Sci. Appl.* **2018**, *7*, 87. [CrossRef]
50. Wang, G.; Zhang, D.; Li, J.; Gan, G.; Rao, Y.; Huang, X.; Yang, Y.; Shi, L.; Liao, Y.; Liu, C.; et al. Crystal Structure, Bond Energy, Raman Spectra, and Microwave Dielectric Properties of Ti-Doped $Li_3Mg_2NbO_6$ Ceramics. *J. Am. Ceram. Soc.* **2020**, *103*, 4321–4332. [CrossRef]
51. Tamura, H. Microwave Dielectric Losses Caused by Lattice Defects. *J. Eur. Ceram. Soc.* **2006**, *26*, 1775–1780. [CrossRef]
52. Kim, W.S.; Kim, E.S.; Yoon, K.H. Effects of Sm^{3+} Substitution on Dielectric Properties of $Ca_{1-x}Sm_{2x/3}TiO_3$ Ceramics at Microwave Frequencies. *J. Am. Ceram. Soc.* **1999**, *82*, 2111–2115. [CrossRef]